Study on the Composite Electromagnetic Scattering from 3D Conductor Multi-Objects above the Rough Surface

Ting LIU[1,2], Lin ZHANG[1], Zhi-Guo ZENG[1,2], Sheng-Jun WEI[3]

[1] Dept. of Air and Missile Defense College, University of Air Force Engineering University, Xi'an, China
[2]Hunan University of Science and Technology, Xiangtan, China
[3] Troops of 95100, Guangzhou, China

gltian163@163.com

Submitted May 26, 2020 / Accepted December 29, 2020

Abstract. *The traditional algorithm for the composite electromagnetic scattering from 3D conductor multi-objects above the rough surface has such weaknesses as slow computation speed and large memory consumption. On the basis of the fast algorithm integrated with the traditional coupling method of moment and physical optics method (MoM-PO), this paper uses the multilevel fast multipole method (MLFMA) and fast far-field approximation (FAFFA) to accelerate the multiplication of matrix vector between the object and environment, which greatly improves the computation speed and reduces the memory consumption. This paper adopts the dual Debye sweater permittivity model to simulate the real sea surface environment, establishes the coupling MoM-PO model of composite scattering from multi-objects on and above the sea surface, and obtains the composite electromagnetic scattering coefficient in virtue of the interaction between object area and rough surface area calculated by the MLFMA and FAFFA. The changes of composite scattering coefficient along with the change of object spacing, size, incident angles, tilt angle, type and sea surface wind speed are also analyzed in detail. The computation results show that the hybrid method consisting of the method of moment accelerated by MLFMA and FAFFA and physical optics method brings higher accuracy and computation efficiency (the computation time and memory consumption are 62% and 82% of the method of moment respectively).*

Keywords

Hybrid method, 3D multiple targets, composite scattering

1. Introduction

Composite scattering characteristic from object and environment plays a key role in features remote sensing, radar detection, object tracking, etc. [1–5]. In civilian use, remote sensing radar can obtain parameters such as sea surface wind speed, temperature, salinity, surface roughness, and soil humidity, etc. by measuring the electromagnetic scattering coefficient in the background of sea and ground object [6]. In military use, the hedgehopping military objects, such as missiles and fighter aircrafts, can cover their echoes using the ground clutter and multipath signals generated by the coupling of the object and the environment, thus avoiding radar tracking. Composite scattering characteristics of the object and environment are also badly needed for the detection of chariots in jungles and underground objects [7], [8]. However, the objects in the actual background often appear simultaneously with multiple objects. In view of the above background, it is of great significance to study the composite scattering from object and environment under the background of ground object and sea.

The traditional methods for calculating the composite electromagnetic scattering characteristics from object and environment include numerical algorithms such as the method of moment [9] and numerical algorithms that have been improved a lot [10–12]. With numerical algorithm, the interaction between all surface elements must be calculated and the accuracy is very high. Finally, it is generally used for electromagnetic scattering analysis of electrically small objects. However, if the number of unknowns sharply increases along with a larger number of objects and a large size of object and environment, the numerical algorithm requires huge computation memory and the computation efficiency is extremely low, making it hard to solve the composite electromagnetic scattering from object and environment. Analytic algorithms have been extensively applied into engineering practice, such as ray tracing algorithms which include geometry optic (GO) [13], uniform theory of diffraction (UTD) [14], shooting-and-bouncing ray (SBR) [15], etc., and high-frequency algorithms consisting of iterative physical optic (IPO) [16], [17], multiple reflection physical optic (MRPO) [18]. The ray tracing algorithms entail accurate ray tracking. For the very complex object structure the spurious diffraction effect will occur by abrupt shadow edge, causing a large computation error. The iterative high-frequency algorithm, which is not as efficient as the ray tracing algorithm, calculates the induced current on the object surface by establishing the electromagnetic field equation. It boasts higher computa-

tion accuracy. However, when analyzing multi-objects interactions, the iteration does not converge or converges quite slowly. The analytical-numerical hybrid algorithm developed in recent years effectively combines the advantages of numerical and analytical algorithms. By calculating the complex objects with numerical method, it uses analytic algorithm to solve the large and simple environment and calculates coupling scattering field by mutual iteration or by coupling the environment scattering into the object impedance matrix. The analytical-numerical hybrid algorithm with a higher computation accuracy and speed includes a hybrid algorithm integrated with method of moment and Kirchhoff approximation (KA) [19], hybrid algorithm integrated with finite element method- Boundary integral method (FE-BI) and physical optics [20], hybrid algorithm integrated with small perturbation method (SPM) and method of moment [21], etc. The hybrid algorithm integrated with FE-BI and physical optics is mainly aimed at the composite scattering from object and environment with inhomogeneous media. According to this method, an integral equation is established inside the object, resulting in more unknowns and low computation efficiency. SPM is only applicable to the environment with micro roughness and has a large computation error. The MoM-PO hybrid algorithm has a higher computation accuracy and efficiency by establishing an integral equation on the object surface and using physical optics to approximately calculate the equivalent induced current above the rough surface of the large rough surface. The MoM-PO hybrid algorithm includes two types of computation methods: Iterative MoM-PO hybrid algorithm [22], [23] and coupling MoM-PO hybrid algorithm [19], [24]. To be specific, the former separately calculates the scattering of the MoM area and the PO area, and interaction between the object and the environment is obtained by iterating each other. By contrast, the latter couples the scattering contribution of the PO area into the impedance matrix of the MoM area. The scattering from object and environment is calculated as a whole. Coupling MoM-PO considers all scattering contributions between objects and also between object and environment, and has higher computation accuracy. When the incident wavelength is fitted to the environment scale, the object and environment should be calculated as a whole [19]. However, when the number of objects increases, the environment scale to be calculated also increases accordingly, and the number of unknowns of the entire area increases exponentially. According to the traditional MoM-PO hybrid algorithm, it is very time-consuming to calculate the interactions of all elements between object and environment while calculating the coupling between them. To improve the efficiency of the coupling between the object area and the rough surface area effectively, Tian Guilong et al. [25] introduced the fast far-field approximation (FAFFA) into the computation of the coupling effect between the object and environment. The interaction enabled by the FAFFA between two groups of surface elements with a long distance is realized by "polymerization – transfer – depolymerization", to avoid the direct interaction between the two groups of surface elements. It further simplifies the MLFMA algorithm and makes transfer by calculating the direction from the field group center to the source group center alone, improving computation efficiency. Certainly, when the object is close to the environment, most of the environment cannot meet the FFA conditions, and the computation efficiency can be hardly improved greatly. Cui et al. [26] suggested combining MLFMA and FAFFA for the computation of the scattering field of electrically large objects and using FAFFA for calculating the area that meets the FFA conditions and MLFMA for accelerating for the area that does not meet the conditions. In this paper, MLFMA-FAFFA is introduced into the matrix vector multiplication of object surface element and environment surface element. According to the FFA conditions, the environment is divided into the near area and the far area. The coupling between the near environment and the object is accelerated by MLFMA, and that of the far environment is accelerated by FAFFA.

As the traditional coupling MoM-PO cannot effectively calculate the composite scattering from object and environment, this paper uses MLFMA and FAFFA to improve the coupling MoM-PO and obtain a new accelerated MoM-PO hybrid algorithm. This paper establishes the coupling MoM-PO model first and then accelerates the coupling impedance matrix using MLFMA and FAFFA; the composite electromagnetic scattering coefficient is obtained through computation. Afterwards, the changes of the composite scattering characteristics from multi-objects conductors on and above the sea surface along with the object spacing, size, incident angles, tilt angle, types and sea surface wind speed are analyzed in detail. According to the computation results, compared with the traditional method of moment and the hybrid method integrated with method of moment and physical optics method, the algorithm improved in this paper has higher accuracy and efficiency.

2. Coupling MoM-PO Hybrid Algorithm

Figure 1 shows a schematic diagram of multi-objects conductor above the rough sea surface. S_{tk}^{mom} is the k-th object in the MoM area, and the object size is $\pi\lambda^2 \cdot l$; S_{r}^{po} is the rough sea surface, and the size of sea surface is $L_{\text{x}} \times L_{\text{y}}$; the spacing between objects is d, and the height of the object from the sea surface is H. $\boldsymbol{k}_{\text{i}}$ is the incident wave vector, $(\theta_{\text{i}}, \varphi_{\text{i}})$ is the incident angle, and $(\theta_{\text{s}}, \varphi_{\text{s}})$ is scattering angle. The object and environment are divided into the MoM area and the PO area respectively. The electromagnetic flow on the surface of the MoM area is calculated using the method of moment while that on the surface of the PO area is calculated using physical optics approximation technology. The current coefficient on the surface of MoM area is taken as an unknown, the electromagnetic flow on the surface of PO area is induced by the object scat-

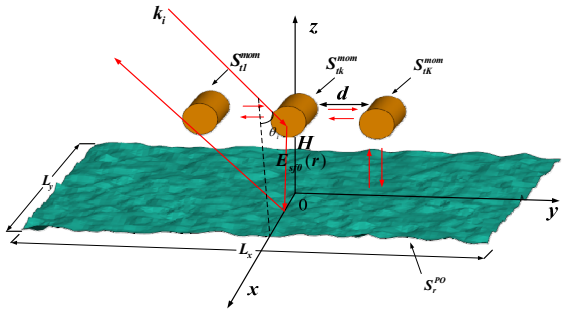

Fig. 1. Schematic diagram of 3D conductor multi-objects's location above 2D sea surface.

tering and the external incident field, and the scattering field generated by equivalent induced electromagnetic flow in the PO area and external incident field are taken as the scattering on object surface. The scattering contribution in PO area is coupled into the impendence matrix of MoM area. The object surface current coefficient is solved to further obtain the composite scattering field from object and environment.

2.1 Object Scattering

The object surface current is expressed by the Rao-Wilton-Glisson (RWG) function. The k^{th} object is discretized into N_k triangular surface elements. The current on the object surface S_{tk}^{mom} is $\boldsymbol{J}_{tk}$, which is expressed as

$$\boldsymbol{J}_{tk}=\sum_{n=1}^{N_k}\alpha_{kn}\boldsymbol{f}_{kn}\ ,k=1,2,...,K \tag{1}$$

where α_{kn} is the current coefficient on the object surface S_{tk}^{mom}, $\boldsymbol{f}_{kn}$ is RWG basic function. The scattering field stimulated by the equivalent induced current on the object surface in free space can be expressed as

$$\boldsymbol{E}_{tk}^{\text{s}}=L^{\text{e}}(\boldsymbol{J}_{\text{tk}}),k=1,2,...,K \tag{2}$$

where L^{e} is expressed as

$$L^{e}(\boldsymbol{J}(\boldsymbol{r}'))=\mathrm{i}k\eta\int_{S}(\overline{\overline{\boldsymbol{I}}}+\frac{\nabla\nabla'}{k^2})\boldsymbol{J}(\boldsymbol{r}')g(\boldsymbol{r},\boldsymbol{r}')\mathrm{d}\boldsymbol{s}' \tag{3}$$

where $\overline{\overline{\boldsymbol{I}}}$ is the unit dyad, $k=\omega\sqrt{\mu_0\cdot\varepsilon_0}$ is the wave number in free space, and $g(\boldsymbol{r},\boldsymbol{r}')=\exp(-\mathrm{j}k|\boldsymbol{r}-\boldsymbol{r}'|/(4\pi|\boldsymbol{r}-\boldsymbol{r}'|)$ is the Green's function in free space. Then the scattering field generated by the surface currents of objects region is expressed as

$$\boldsymbol{E}_{\text{t}}^{\text{s}}=\sum_{k=1}^{K}L^{\text{e}}(\boldsymbol{J}_{\text{tk}})=\sum_{k=1}^{K}\sum_{n=1}^{N_k}\alpha_{kn}L^{\text{e}}(\boldsymbol{f}_{kn}). \tag{4}$$

2.2 Environment Scattering

According to Huygens principle, when the incident field is $\boldsymbol{E}_{\text{i}}$, the electric field scattered on the rough surface can be expressed as

$$\begin{aligned}\boldsymbol{E}_{\text{s}}(\boldsymbol{r})&=K^{\text{e}}(\boldsymbol{J}_{\text{S}}(\boldsymbol{r}'),\boldsymbol{M}_{\text{S}}(\boldsymbol{r}'))\\&=\int_{s}\mathrm{d}s'\,\mathrm{i}k\eta(\overline{\overline{\boldsymbol{I}}}+\frac{\nabla\nabla'}{k^2})g(\boldsymbol{r},\boldsymbol{r}')\cdot\boldsymbol{J}_{\text{S}}(\boldsymbol{r}')\\&\quad+\int_{s}\mathrm{d}s'\,\nabla g(\boldsymbol{r},\boldsymbol{r}')\times\boldsymbol{M}_{\text{S}}(\boldsymbol{r}').\end{aligned} \tag{5}$$

When the local incident angle on the rough surface satisfies $\cos\theta_{\text{i}}=-\hat{\boldsymbol{n}}\cdot\boldsymbol{k}_{\text{i}}$, a local coordinate system of $(\hat{\boldsymbol{p}},\hat{\boldsymbol{q}},\hat{\boldsymbol{k}})$ can be established, whose horizontal and vertical polarization can be expressed as

$$\hat{\boldsymbol{q}}=\frac{\boldsymbol{k}_i\times\hat{\boldsymbol{n}}}{|\boldsymbol{k}_i\times\hat{\boldsymbol{n}}|},\ \hat{\boldsymbol{p}}=\hat{\boldsymbol{q}}\times\hat{\boldsymbol{k}}\ . \tag{6}$$

The horizontal and vertical polarization components of the incident electric and magnetic fields can be expressed as

$$\begin{aligned}&\boldsymbol{E}_{\text{i}}^{\text{h}}=(\hat{\boldsymbol{q}}\cdot\boldsymbol{E}_{\text{i}})\hat{\boldsymbol{h}},\ \boldsymbol{H}_{\text{i}}^{\text{v}}=\frac{1}{\eta}\boldsymbol{k}_{\text{i}}\times\boldsymbol{E}_{\text{i}}^{\text{h}},\\&\boldsymbol{H}_{\text{i}}^{\text{h}}=(\hat{\boldsymbol{q}}\cdot\boldsymbol{H}_{\text{i}})\hat{\boldsymbol{h}},\ \boldsymbol{E}_{\text{i}}^{\text{v}}=\eta\boldsymbol{H}_{\text{i}}^{\text{h}}\times\hat{\boldsymbol{k}}.\end{aligned} \tag{7}$$

When the radius of curvature of the rough surface and the incident wavelength satisfy the condition $\rho>>\lambda$, then the environment can be made approximate to consist of countless planes. According to the tangent plane approximate, the local reflection direction is: $\hat{\boldsymbol{k}}_{\text{r}}=\hat{\boldsymbol{k}}_{\text{i}}-2\hat{\boldsymbol{n}}(\hat{\boldsymbol{n}}\cdot\boldsymbol{k}_{\text{i}})$; if partial reflected electric field and reflected magnetic field satisfy the TEM right handgrip rule, then the polarization vector of the reflected electric field and magnetic field can be expressed as

$$\begin{aligned}&\boldsymbol{E}_{\text{r}}^{\text{h}}=R^{\text{TE}}\boldsymbol{E}_{\text{i}}^{\text{h}},\ \boldsymbol{H}_{\text{r}}^{\text{v}}=\frac{1}{\eta}\hat{\boldsymbol{k}}_{\text{r}}\times\boldsymbol{E}_{\text{r}}^{\text{h}},\\&\boldsymbol{H}_{\text{r}}^{\text{h}}=R^{\text{TM}}\boldsymbol{H}_{\text{i}}^{\text{h}},\ \boldsymbol{E}_{\text{r}}^{\text{v}}=\eta\boldsymbol{H}_{\text{r}}^{\text{h}}\times\hat{\boldsymbol{k}}_{\text{r}}\end{aligned} \tag{8}$$

where R^{TE} and R^{TM} are respectively the Fresnel reflection coefficient under the approximation condition of tangent plane. Then the electric field $\boldsymbol{E}$ and magnetic field $\boldsymbol{H}$ on the rough surface can be expressed as

$$\begin{aligned}&\boldsymbol{E}=(1+R^{\text{TE}})\boldsymbol{E}_{\text{i}}^{\text{h}}+\eta[\boldsymbol{H}_{\text{i}}^{\text{h}}\times\hat{\boldsymbol{k}}_{\text{i}}+R^{\text{TM}}\boldsymbol{H}_{\text{i}}^{\text{h}}\times\hat{\boldsymbol{k}}_{\text{r}}],\\&\boldsymbol{H}=(1+R^{\text{TM}})\boldsymbol{H}_{\text{i}}^{\text{h}}+\frac{1}{\eta}[\hat{\boldsymbol{k}}_{\text{i}}\times\boldsymbol{E}_{\text{i}}^{\text{h}}+R^{\text{TE}}\hat{\boldsymbol{k}}_{\text{r}}\times\boldsymbol{E}_{\text{i}}^{\text{h}}].\end{aligned} \tag{9}$$

It can be further expressed as

$$\begin{aligned}&\boldsymbol{E}=(1+R^{\text{TE}})(\hat{\boldsymbol{q}}\cdot\boldsymbol{E}_{\text{i}})\hat{\boldsymbol{q}}+(\hat{\boldsymbol{p}}\cdot\boldsymbol{E}_{\text{i}})[\hat{\boldsymbol{p}}-R^{\text{TM}}\hat{\boldsymbol{k}}_{\text{r}}\times\hat{\boldsymbol{q}}],\\&\boldsymbol{H}=\frac{(\hat{\boldsymbol{p}}\cdot\boldsymbol{E}_{\text{i}})}{\eta}(1+R^{\text{TM}})\hat{\boldsymbol{q}}-\frac{(\hat{\boldsymbol{q}}\cdot\boldsymbol{E}_{\text{i}})}{\eta}[\hat{\boldsymbol{p}}-R^{\text{TM}}\hat{\boldsymbol{k}}_{\text{r}}\times\hat{\boldsymbol{q}}].\end{aligned} \tag{10}$$

The direct equivalent induced electric current $\boldsymbol{J}_{\text{S0}}(\boldsymbol{r})$ and equivalent induced magnetic current $\boldsymbol{M}_{\text{S0}}(\boldsymbol{r})$ stimulated by the incident field $\boldsymbol{E}^{\text{inc}}$ on the rough surface can be expressed as

$$\begin{aligned}\boldsymbol{J}_{\text{S0}}(\boldsymbol{r})&=\hat{\boldsymbol{n}}\times\boldsymbol{H}_{1}(\boldsymbol{r})\\&=\hat{\boldsymbol{n}}\times\left\{\frac{(\hat{\boldsymbol{p}}\cdot\boldsymbol{E}^{\text{inc}})}{\eta}(1+R^{\text{TM}})\hat{\boldsymbol{q}}-\frac{(\hat{\boldsymbol{q}}\cdot\boldsymbol{E}^{\text{inc}})}{\eta}[\hat{\boldsymbol{p}}-R^{\text{TM}}\hat{\boldsymbol{k}}_{\text{r}}\times\hat{\boldsymbol{q}}]\right\},\end{aligned}$$

$$\begin{aligned}\boldsymbol{M}_{\mathrm{S0}}(\boldsymbol{r}) &= -\hat{\boldsymbol{n}}\times\boldsymbol{E}_1(\boldsymbol{r})\\ &= -\hat{\boldsymbol{n}}\times\left\{(1+R^{\mathrm{TE}})(\hat{\boldsymbol{q}}\cdot\boldsymbol{E}^{\mathrm{inc}})\hat{\boldsymbol{q}}+(\hat{\boldsymbol{p}}\cdot\boldsymbol{E}^{\mathrm{inc}})[\hat{\boldsymbol{p}}-R^{\mathrm{TM}}\hat{\boldsymbol{k}}_{\mathrm{r}}\times\hat{\boldsymbol{q}}]\right\}\end{aligned} \tag{11}$$

where $\boldsymbol{E}_1(\boldsymbol{r})$ and $\boldsymbol{H}_1(\boldsymbol{r})$ are induced electric field and magnetic field stimulated by the external incident field on the rough surface, and $\hat{\boldsymbol{n}}$ is the local normal vectors. The induced electric current $\boldsymbol{J}_{\mathrm{Sd}}(\boldsymbol{r})$ and magnetic current $\boldsymbol{M}_{\mathrm{Sd}}(\boldsymbol{r})$ generated by the scattering field $\boldsymbol{E}_{\mathrm{tk}}{}^{\mathrm{s}}$ on the rough surface are respectively expressed as

$$\begin{aligned}\boldsymbol{J}_{\mathrm{Sd}}(\boldsymbol{r}) &= \hat{\boldsymbol{n}}\times\boldsymbol{H}_2(\boldsymbol{r})\\ &= \hat{\boldsymbol{n}}\times\left\{\frac{1}{\eta}(\hat{\boldsymbol{p}}\cdot\boldsymbol{E}_{\mathrm{t}}^{\mathrm{s}})(1+R^{\mathrm{TM}})\hat{\boldsymbol{q}}-\frac{1}{\eta}(\hat{\boldsymbol{q}}\cdot\boldsymbol{E}_{\mathrm{t}}^{\mathrm{s}})[\hat{\boldsymbol{p}}-R^{\mathrm{TM}}\hat{\boldsymbol{k}}_{\mathrm{r}}\times\hat{\boldsymbol{q}}]\right\},\\ \boldsymbol{M}_{\mathrm{Sd}}(\boldsymbol{r}) &= -\hat{\boldsymbol{n}}\times\boldsymbol{E}_2(\boldsymbol{r})\\ &= -\hat{\boldsymbol{n}}\times\left\{(1+R^{\mathrm{TE}})(\hat{\boldsymbol{q}}\cdot\boldsymbol{E}_{\mathrm{t}}^{\mathrm{s}})\hat{\boldsymbol{q}}+(\hat{\boldsymbol{p}}\cdot\boldsymbol{E}_{\mathrm{t}}^{\mathrm{s}})[\hat{\boldsymbol{p}}-R^{\mathrm{TM}}\hat{\boldsymbol{k}}_{\mathrm{r}}\times\hat{\boldsymbol{q}}]\right\}\end{aligned} \tag{12}$$

where $\boldsymbol{E}_2(\boldsymbol{r})$ and $\boldsymbol{H}_2(\boldsymbol{r})$ are the induced electromagnetic fields stimulated by the scattering field $\boldsymbol{E}_{\mathrm{t}k}{}^{\mathrm{s}}$ on the rough surface. The total induced electromagnetic currents on the rough surface can be expressed as

$$\begin{aligned}\boldsymbol{J}_{\mathrm{S}}(\boldsymbol{r}) &= \boldsymbol{J}_{\mathrm{Sd}}(\boldsymbol{r})+\boldsymbol{J}_{\mathrm{S0}}(\boldsymbol{r}),\\ \boldsymbol{M}_{\mathrm{S}}(\boldsymbol{r}) &= \boldsymbol{M}_{\mathrm{Sd}}(\boldsymbol{r})+\boldsymbol{M}_{\mathrm{S0}}(\boldsymbol{r}).\end{aligned} \tag{13}$$

The total scattering electric field $\boldsymbol{E}_{\mathrm{s}}$ from rough surface impacting on target $S_k{}^{\mathrm{mom}}$ can be expressed as

$$\begin{aligned}\boldsymbol{E}_{\mathrm{S}}(\boldsymbol{r}_k) &= \boldsymbol{E}_{\mathrm{S0}}(\boldsymbol{r}_k,\boldsymbol{r}_{\mathrm{s}}')+\boldsymbol{E}_{\mathrm{Sd}}(\boldsymbol{r}_{\mathrm{k}},\boldsymbol{r}_{\mathrm{s}}')\\ &= K^{\mathrm{e}}(\boldsymbol{J}_{\mathrm{S0}}(\boldsymbol{r}_{\mathrm{s}}'),\boldsymbol{M}_{\mathrm{S0}}(\boldsymbol{r}_{\mathrm{s}}'))+K^{\mathrm{e}}(\boldsymbol{J}_{\mathrm{Sd}}(\boldsymbol{r}_{\mathrm{s}}'),\boldsymbol{M}_{\mathrm{Sd}}(\boldsymbol{r}_{\mathrm{s}}'))\end{aligned} \tag{14}$$

where $\boldsymbol{E}_{\mathrm{S0}}$ is the direct scattering electric field caused by the external incident field $\boldsymbol{E}^{\mathrm{inc}}$ on the rough surface, and $\boldsymbol{E}_{\mathrm{Sd}}(\boldsymbol{r})$ is the scattering electric field caused by the incident field $\boldsymbol{E}^{\mathrm{s}}{}_{tk}$ on the rough surface.

2.3 Coupling Scattering of Object and Environment

The scattering field $\boldsymbol{E}^{\mathrm{S}}(\boldsymbol{r}_k)$ on the surface of object $S_k{}^{\mathrm{mom}}$ is composed of the scatting electric field stimulated by the object's equivalent induced electric current, the scattering field caused by other object's equivalent induced electric current, and the scattering electric field caused by the electromagnetic current on the rough surface. $\boldsymbol{E}^{\mathrm{S}}(\boldsymbol{r}_k)$ can be expressed as

$$\begin{aligned}\boldsymbol{E}^{\mathrm{S}}(\boldsymbol{r}_k) &= \boldsymbol{E}_{\mathrm{t}k}^{\mathrm{S}}(\boldsymbol{r}_k)+\sum_{i=1,i\neq k}^{K}\boldsymbol{E}_{\mathrm{t}i}^{\mathrm{S}}(\boldsymbol{r}_k)+\boldsymbol{E}_{\mathrm{S}}(\boldsymbol{r}_k)\\ &= L^{\mathrm{e}}(\boldsymbol{J}_{\mathrm{t}k})+\sum_{i=1,i\neq k}^{K}L^{\mathrm{e}}(\boldsymbol{J}_{\mathrm{t}i})+K^{\mathrm{e}}(\boldsymbol{J}_{\mathrm{S}},\boldsymbol{M}_{\mathrm{S}}).\end{aligned} \tag{15}$$

When the incident wave is vertically polarized, based on Dirichlet boundary conditions, the electric field integral equation on the surface of conductor target can be expressed as

$$\boldsymbol{E}_{\tan} = \boldsymbol{E}^{\mathrm{inc}}+\boldsymbol{E}^{\mathrm{S}}\big|_{\tan} = 0 \tag{16}$$

where $\boldsymbol{E}^{\mathrm{inc}}$ is externally incident electric field, $\boldsymbol{E}^{\mathrm{S}}$ is scattering electric field in free space. By substituting (15) into (16), a new formula can be obtained as below

$$\begin{aligned}0 &= \sum_{i=1,i\neq k}^{K}L^{\mathrm{e}}[\boldsymbol{J}_{\mathrm{t}i}(\boldsymbol{r}_i')]+K^{\mathrm{e}}[\boldsymbol{J}_{\mathrm{S0}}(\boldsymbol{r}_{\mathrm{s}}'),\boldsymbol{M}_{\mathrm{S0}}(\boldsymbol{r}_{\mathrm{s}}')]+K^{\mathrm{e}}[\boldsymbol{J}_{\mathrm{Sd}}(\boldsymbol{r}_{\mathrm{s}}'),\boldsymbol{M}_{\mathrm{Sd}}(\boldsymbol{r}_{\mathrm{s}}')]\Big|_{\tan}\\ &\quad+\boldsymbol{E}^{\mathrm{inc}}(\boldsymbol{r}_k)+L^{\mathrm{e}}[\boldsymbol{J}_{\mathrm{t}k}(\boldsymbol{r}_k)],\\ &(\boldsymbol{r}_k\in\boldsymbol{S}_k^{\mathrm{mom}},k=1,2,...,K).\end{aligned} \tag{17}$$

It can be further rewritten as

$$\begin{aligned}&-\left[L^{\mathrm{e}}[\boldsymbol{J}_{\mathrm{t}1}(\boldsymbol{r}_1)]+\sum_{i=2}^{K}L^{\mathrm{e}}[\boldsymbol{J}_{\mathrm{t}i}(\boldsymbol{r}_i')]+K^{\mathrm{e}}[\boldsymbol{J}_{\mathrm{Sd}}(\boldsymbol{r}_{\mathrm{s}}'),\boldsymbol{M}_{\mathrm{Sd}}(\boldsymbol{r}_{\mathrm{s}}')]\right]_{\tan}\\ &=\left[\boldsymbol{E}^{\mathrm{inc}}(\boldsymbol{r}_1)+K^{\mathrm{e}}[\boldsymbol{J}_{\mathrm{S0}}(\boldsymbol{r}_{\mathrm{s}}'),\boldsymbol{M}_{\mathrm{S0}}(\boldsymbol{r}_{\mathrm{s}}')]\right]_{\tan},\\ &\cdots\\ &-\left[L^{\mathrm{e}}[\boldsymbol{J}_{\mathrm{t}k}(\boldsymbol{r}_k)]+\sum_{i=1,i\neq k}^{K}L^{\mathrm{e}}[\boldsymbol{J}_{\mathrm{t}i}(\boldsymbol{r}_i')]+K^{\mathrm{e}}[\boldsymbol{J}_{\mathrm{Sd}}(\boldsymbol{r}_{\mathrm{s}}'),\boldsymbol{M}_{\mathrm{Sd}}(\boldsymbol{r}_{\mathrm{s}}')]\right]_{\tan}\\ &=\left[\boldsymbol{E}^{\mathrm{inc}}(\boldsymbol{r}_k)+K^{\mathrm{e}}[\boldsymbol{J}_{\mathrm{S0}}(\boldsymbol{r}_{\mathrm{s}}'),\boldsymbol{M}_{\mathrm{S0}}(\boldsymbol{r}_{\mathrm{s}}')]\right]_{\tan},\\ &\cdots\\ &-\left[L^{\mathrm{e}}[\boldsymbol{J}_{\mathrm{t}K}(\boldsymbol{r}_K)]+\sum_{i=1}^{K-1}L^{\mathrm{e}}[\boldsymbol{J}_{\mathrm{t}i}(\boldsymbol{r}_i')]+K^{\mathrm{e}}[\boldsymbol{J}_{\mathrm{Sd}}(\boldsymbol{r}_{\mathrm{s}}'),\boldsymbol{M}_{\mathrm{Sd}}(\boldsymbol{r}_{\mathrm{s}}')]\right]_{\tan}\\ &=\left[\boldsymbol{E}^{\mathrm{inc}}(\boldsymbol{r}_K)+K^{\mathrm{e}}[\boldsymbol{J}_{\mathrm{S0}}(\boldsymbol{r}_{\mathrm{s}}'),\boldsymbol{M}_{\mathrm{S0}}(\boldsymbol{r}_{\mathrm{s}}')]\right]_{\tan},\\ &(\boldsymbol{r}_k\in\boldsymbol{S}_k^{\mathrm{mom}},k=1,2,...,K).\end{aligned} \tag{18}$$

The following formulas can be obtained through testing using Galerkin method

$$\begin{aligned}&-\left\langle L^{\mathrm{e}}[\boldsymbol{J}_{\mathrm{t}1}(\boldsymbol{r}_1)]+\sum_{i=2}^{K}L^{\mathrm{e}}[\boldsymbol{J}_{\mathrm{t}i}(\boldsymbol{r}_i')]+K^{\mathrm{e}}[\boldsymbol{J}_{\mathrm{Sd}}(\boldsymbol{r}_{\mathrm{s}}'),\boldsymbol{M}_{\mathrm{Sd}}(\boldsymbol{r}_{\mathrm{s}}')],\boldsymbol{f}_{1m}\right\rangle_{\tan}\\ &=\left\langle\boldsymbol{E}^{\mathrm{inc}}(\boldsymbol{r}_1),\boldsymbol{f}_{1m}\right\rangle_{\tan}+\left\langle K^{\mathrm{e}}[\boldsymbol{J}_{\mathrm{S0}}(\boldsymbol{r}_{\mathrm{s}}'),\boldsymbol{M}_{\mathrm{S0}}(\boldsymbol{r}_{\mathrm{s}}')],\boldsymbol{f}_{1m}\right\rangle_{\tan},\\ &\cdots\\ &-\left\langle L^{\mathrm{e}}[\boldsymbol{J}_{\mathrm{t}k}(\boldsymbol{r}_k)]+\sum_{i=1,i\neq k}^{K}L^{\mathrm{e}}[\boldsymbol{J}_{\mathrm{t}i}(\boldsymbol{r}'_i)]+K^{\mathrm{e}}[\boldsymbol{J}_{\mathrm{Sd}}(\boldsymbol{r}_{\mathrm{s}}'),\boldsymbol{M}_{\mathrm{Sd}}(\boldsymbol{r}_{\mathrm{s}}')],\boldsymbol{f}_{km}\right\rangle_{\tan}\\ &=\left\langle\boldsymbol{E}^{\mathrm{inc}}(\boldsymbol{r}_k),\boldsymbol{f}_{km}\right\rangle_{\tan}+\left\langle K^{\mathrm{e}}[\boldsymbol{J}_{\mathrm{S0}}(\boldsymbol{r}_{\mathrm{s}}'),\boldsymbol{M}_{\mathrm{S0}}(\boldsymbol{r}_{\mathrm{s}}')],\boldsymbol{f}_{km}\right\rangle_{\tan},\\ &\cdots\\ &-\left\langle L^{\mathrm{e}}[\boldsymbol{J}_{\mathrm{t}K}(\boldsymbol{r}_K)]+\sum_{i=1}^{K-1}L^{\mathrm{e}}[\boldsymbol{J}_{\mathrm{t}i}(\boldsymbol{r}'_i)]+K^{\mathrm{e}}[\boldsymbol{J}_{\mathrm{Sd}}(\boldsymbol{r}_{\mathrm{s}}'),\boldsymbol{M}_{\mathrm{Sd}}(\boldsymbol{r}_{\mathrm{s}}')],\boldsymbol{f}_{Km}\right\rangle_{\tan}\\ &=\left\langle\boldsymbol{E}^{\mathrm{inc}}(\boldsymbol{r}_K),\boldsymbol{f}_{Km}\right\rangle_{\tan}+\left\langle K^{\mathrm{e}}[\boldsymbol{J}_{\mathrm{S0}}(\boldsymbol{r}_{\mathrm{s}}'),\boldsymbol{M}_{\mathrm{S0}}(\boldsymbol{r}_{\mathrm{s}}')],\boldsymbol{f}_{Km}\right\rangle_{\tan},\\ &(\boldsymbol{r}_k\in\boldsymbol{S}_k^{\mathrm{mom}},k=1,2,...,K)\end{aligned} \tag{19}$$

where the inner product of the vector is defined as $\langle\boldsymbol{f},\boldsymbol{g}\rangle=\int_s\boldsymbol{f}\cdot\boldsymbol{g}\,\mathrm{d}s$. This equation can be simplified as

$$\begin{aligned}
&\left[\boldsymbol{Z}_{mn}^{1}+\boldsymbol{Z}_{mn}^{1\mathrm{t}}+\boldsymbol{Z}_{mn}^{1\mathrm{S}}\right]\cdot\left[\boldsymbol{\alpha}_{1}\right]=\left[\boldsymbol{V}_{1}^{\mathrm{inc}}+\boldsymbol{V}_{1}^{\mathrm{S}}\right],\\
&\cdots\\
&\left[\boldsymbol{Z}_{mn}^{k}+\boldsymbol{Z}_{mn}^{k\mathrm{t}}+\boldsymbol{Z}_{mn}^{k\mathrm{S}}\right]\cdot\left[\boldsymbol{\alpha}_{k}\right]=\left[\boldsymbol{V}_{k}^{\mathrm{inc}}+\boldsymbol{V}_{k}^{\mathrm{S}}\right],\\
&\cdots\\
&\left[\boldsymbol{Z}_{mn}^{K}+\boldsymbol{Z}_{mn}^{K\mathrm{t}}+\boldsymbol{Z}_{mn}^{KS}\right]\cdot\left[\boldsymbol{\alpha}_{K}\right]=\left[\boldsymbol{V}_{K}^{\mathrm{inc}}+\boldsymbol{V}_{K}^{\mathrm{S}}\right]
\end{aligned}\tag{20}$$

where $\boldsymbol{Z}^{k}_{mn}$ is the self-impedance matrix on the surface of the object S_{tk}^{mom}, $\boldsymbol{Z}^{kt}_{mn}$ is the mutual impedance matrix of the object S_{tk}^{mom} and other objects, $\boldsymbol{Z}^{kS}_{mn}$ is the mutual impedance matrix of the object and the environment, $\boldsymbol{V}_{m}^{\mathrm{inc}}$ is the stimulation vector caused by the external incident field's direct irradiation on the object on the object surface and $\boldsymbol{V}_{m}^{\mathrm{S}}$ is the stimulation vector caused by the external incident field's irradiation to the environment and then the radiation of the scattering field stimulated on the environment to the object.

By solving (20), the object surface current coefficient α_1, α_2, …,α_K (k = 1,2,…,K) can be obtained and the object surface current is obtained by (1). The environment electromagnetic current are obtained by solving (11). (12). and (13). The bistatic scattering coefficient can be expressed as

$$\sigma_{\alpha\beta}=\lim_{r\to\infty}\frac{4\pi r^{2}\left|\boldsymbol{E}_{\alpha}^{\mathrm{Sur}}+\boldsymbol{E}_{\alpha}^{\mathrm{Tar}}\right|^{2}\cos\theta_{\mathrm{i}}}{\left|\boldsymbol{E}_{\beta}^{\mathrm{i}}\right|^{2}\cdot S\cdot\cos\theta_{\mathrm{i}}}\tag{21}$$

where α is the scattering direction, β is the incident direction, $\boldsymbol{E}_{\alpha}^{\mathrm{Sur}}$ and $\boldsymbol{E}_{\alpha}^{\mathrm{Tar}}$ are the scattering electric field of the environment and the object under polarization respectively, $\boldsymbol{E}_{\beta}^{\mathrm{i}}$ is the incident electric field under β polarization, θ_{i} is the incident angle and S·cos θ_{i} is the projected area of the incident wave under vertical polarization.

3. MLFMA-FAFFA Acceleration Algorithm

In (20), $\boldsymbol{Z}^{kS}_{mn}$ is the interaction impedance matrix between the object and the environment and is obtained by multiplying the matrix vector between the surface element in the MoM area and the PO area. When the method of moment is used for direct computation, the computation complexity is $2M^2P$ [27], M is the number of unknowns in the MoM area and P is the number of unknowns in the PO area. It can be seen that the computation complexity increases sharply as the number of objects increases. Therefore, the MLFMA-FAFFA is used for acceleration.

3.1 Multilevel Fast Multipole Method Technology (MLFMA)

To use the MLFMA algorithm for computation effectively, this paper puts the 3D object S to be calculated into the smallest box which could contain S (the box is called a Level 0 box) and then divides the box into 8 sub-boxes, all of which are taken as Level 1 sub-boxes; each Level 1 sub-box is divided into 8 pieces to obtain 8 Level 2 sub-boxes; Level 2 sub-boxes is divided further until they are finally divided into Level L sub-boxes, the size of which is about 0.2 λ ~ 0.5 λ. An octree structure is built in the process above. Similarly, this paper groups the environment using a quadtree structure. All levels of boxes can be indexed after building the tree structure but only non-empty boxes are recorded.

Two points $\boldsymbol{r}_i$ and $\boldsymbol{r}_j$ are considered in the computation area. To be specific, $\boldsymbol{r}_i$ is the field point in the field group m, and $\boldsymbol{r}_j$ is the source points in the source group n; if $\boldsymbol{r}_m$ and $\boldsymbol{r}_n$ are respectively expressed as the center of the source and field groups, then the space vector from the source point to the field point can be expressed as: $\boldsymbol{r}_{ij}=\boldsymbol{r}_i-\boldsymbol{r}_j=\boldsymbol{r}_{im}+\boldsymbol{r}_{mn}+\boldsymbol{r}_{nj}$. If group m and group n do not overlap or are not similar, then $|\boldsymbol{r}_{im}+\boldsymbol{r}_{nj}|<\boldsymbol{r}_{mn}$. Therefore, the Green's function can be developed and expressed as below using the addition theorem

$$\frac{\mathrm{e}^{\mathrm{i}k|\boldsymbol{r}_i-\boldsymbol{r}_j|}}{|\boldsymbol{r}_i-\boldsymbol{r}_j|}=\frac{\mathrm{i}k}{4\pi}\int\mathrm{d}^{2}\,\hat{\boldsymbol{k}}\,\mathrm{e}^{\mathrm{i}\boldsymbol{k}\cdot(\boldsymbol{r}_{im}+\boldsymbol{r}_{nj})}\,\alpha_{mn}(\hat{\boldsymbol{k}}\cdot\hat{\boldsymbol{r}}_{mn})\tag{22}$$

and gradient of Green's function is

$$\nabla\frac{\mathrm{e}^{\mathrm{i}k_0|\boldsymbol{r}_a-\boldsymbol{r}_b|}}{|\boldsymbol{r}_a-\boldsymbol{r}_b|}=\frac{k}{4\pi}\int_{S_{\mathrm{E}}}d^{2}\hat{\boldsymbol{k}}\,\mathrm{e}^{\mathrm{i}\boldsymbol{k}\cdot(\boldsymbol{r}_{am}-\boldsymbol{r}_{bm'})}\,\alpha(\hat{\boldsymbol{k}}\cdot\hat{\boldsymbol{r}}_{mm'})\tag{23}$$

where the entire integral equation is defined on the unit sphere (Ewald sphere). α_{mn} is the transfer factor, which can be expressed as

$$\alpha_{mn}(\hat{\boldsymbol{k}}\cdot\hat{\boldsymbol{r}}_{mn})=\sum_{l=0}^{L}\mathrm{i}^{L}\,(2l+1)h_{l}^{(1)}(kr_{mn})P_{l}(\hat{\boldsymbol{k}}\cdot\hat{\boldsymbol{r}}_{mn})\tag{24}$$

where $h_l^{(1)}$ is the first-order spherical Hankel function, P_l is the Legendre function, r_{mn} and $\hat{\boldsymbol{r}}_{mn}$ are the distance and direction from m to n, and L is the truncated number of a finite series. The expression is as below

$$L=kD+\beta(kD)^{1/3}.\tag{25}$$

Equation (22) is the basis of the traditional MLFMA. In the MLFMA algorithm, all $\hat{\boldsymbol{k}}$ directions participate in the transfer, so all $\hat{\boldsymbol{k}}$ directions need to undergo sampling computation. The total number of samples on the Ewald sphere is [28]:

$$K=2L^{2}+4.\tag{26}$$

When D = 10λ, the number of samples to be calculated is K = 11,063. It can be seen that it is quite time consuming for transfer computation using MLFMA. In fact, not all sampling directions have the same contribution to the coupling between surface elements, and their beam energy is mainly concentrated near the direction of $\hat{\boldsymbol{k}}=\hat{\boldsymbol{r}}_{mn}$. The further the distance between the field group and the source group, the more concentrated the beam energy. When the

distance between the two sets of surface elements reaches a certain value, the direction of the scattering energy except the direction $\hat{\boldsymbol{k}} = \hat{\boldsymbol{r}}_{mn}$ can be ignored, so FAFFA can be used for further acceleration.

3.2 Fast Far-Field Approximation (FAFFA)

When the group distance $k\boldsymbol{r}_{mn}$ is large enough, the spherical Hankel function can be expressed by a linear expression

$$h_j^{(1)}(kr_{mn}) \sim (-\mathrm{i})^{j+1} \frac{\mathrm{e}^{\mathrm{i}kr_{mn}}}{kr_{mn}},\ kr_{mn} \sim \infty \tag{27}$$

By substituting (27) into (24), a formula can be obtained and expressed as

$$\alpha_{mn}(\hat{\boldsymbol{k}} \cdot \hat{\boldsymbol{r}}_{mn}) \sim -\mathrm{i} \frac{\mathrm{e}^{\mathrm{i}kr_{mn}}}{kr_{mn}} \sum_{j=0}^{\infty} (2j+1) P_j(\hat{\boldsymbol{k}} \cdot \hat{\boldsymbol{r}}_{mn}). \tag{28}$$

Therefore, the Green's function in (22) can be expressed by a spherical coordinate system as

$$\begin{aligned} \frac{\mathrm{e}^{\mathrm{i}k|\mathbf{r}_i - \mathbf{r}_j|}}{|\boldsymbol{r}_i - \boldsymbol{r}_j|} &\sim \frac{1}{4\pi} \frac{\mathrm{e}^{\mathrm{i}kr_{mn}}}{r_{mn}} \int_0^{2\pi} \mathrm{d}\phi_0 \sin\theta_0 \mathrm{e}^{\mathrm{i}k\hat{\boldsymbol{k}}(\boldsymbol{r}_{im} + \boldsymbol{r}_{nj})} f(\cos\theta_0) \\ &= \frac{1}{4\pi} \frac{\mathrm{e}^{\mathrm{i}kr_{mn}}}{r_{mn}} \int_0^{2\pi} \mathrm{d}\phi_0 \int_{-1}^{1} \mathrm{d}u\, \mathrm{e}^{\mathrm{i}k\hat{\boldsymbol{k}}(\boldsymbol{r}_{im} + \boldsymbol{r}_{nj})} f(u) \end{aligned} \tag{29}$$

where

$$f(u) = \sum_{j=0}^{\infty} (2j+1) P_j(u). \tag{30}$$

It can be concluded with the recursive nature of Legendre functions,

$$(j+1) P_{j+1}(u) = (2j+1) u P_j(u) - j P_{j-1}(u) \tag{31}$$

$f(u) = uf(u)$; when $u \neq 1$, $f(u) = 0$; when $u = 1$, $f(u) \to \infty$ can be obtained from (30). Therefore, $f(u)$ is function δ. From the orthogonality of Legendre function, the following can be known

$$\int_{-1}^{1} \mathrm{d}u\, f(u) = \sum_{j=0}^{\infty} (2j+1) \int_{-1}^{1} \mathrm{d}u\, P_j(u) P_0(u) = 2 \cdot \tag{32}$$

Therefore,

$$f(u) = 2\delta(\delta - 1). \tag{33}$$

Because $u = 1$ is corresponding to $\theta_0 = 0$ and $\hat{\boldsymbol{k}} = \hat{\boldsymbol{r}}_{mn}$, then equation (29) can be simplified as

$$\frac{\mathrm{e}^{\mathrm{i}k|\mathbf{r}_i - \mathbf{r}_j|}}{|\mathbf{r}_i - \mathbf{r}_j|} \sim \frac{\mathrm{e}^{\mathrm{i}kr_{mn}}}{r_{mn}} \mathrm{e}^{\mathrm{i}k\hat{\boldsymbol{r}}_{mn} \cdot (\boldsymbol{r}_{im} + \boldsymbol{r}_{nj})} = \frac{\mathrm{i}k}{4\pi} \int_{S_E} \mathrm{d}^2\hat{\boldsymbol{k}}\, \mathrm{e}^{\mathrm{i}k\hat{\boldsymbol{k}} \cdot (\mathbf{r}_{im} + \mathbf{r}_{nj})} \alpha_{mn}^{\mathrm{far}} \tag{34}$$

where

$$\alpha_{mn}^{\mathrm{far}} = 4\pi \frac{\mathrm{e}^{\mathrm{i}kr_{mn}}}{\mathrm{i}kr_{mn}} \delta(\hat{\boldsymbol{k}} - \hat{\boldsymbol{r}}_{mn}). \tag{35}$$

Formula (34) and (35) are expressions for FAFFA. It can be seen that from the field group m to the source group n, the transfer factor only needs to be calculated in one direction $\hat{\boldsymbol{k}} = \hat{\boldsymbol{r}}_{mn}$, which greatly simplifies the computation compared with the MLFMA algorithm.

3.3 MLFMA-FAFFA Combined Algorithm

According to document [26], the FAFFA conditions are

$$r_{mn} \geq 3\gamma \sqrt{(D_x^l)^2 + (D_y^l)^2 + (D_z^l)^2} \tag{36}$$

where l is Level l sub-group, $l \geq 2$ and $3\sqrt{(\mathrm{D}_x^l)^2 + (\mathrm{D}_y^l)^2 + (\mathrm{D}_z^l)^2}$ is the maximum distance between two groups [28] and $\gamma \geq 1$. According to the FFA conditions, the PO area that does not meet the conditions is divided into near area, and MLFMA algorithm is used for solution; the area that meets the conditions is divided into far area, and the FAFFA is used for computation. As the MLFMA needs to calculate all the sampling directions on the Ewald sphere, the transfer computation is time consuming. When the object is close to the environment, it is necessary to calculate the coupling effect on all directions.

However, when the object is far away from the environment, the coupling effect between the object and the environment gradually weakens. The coupling effect between the object and the environment is mainly concentrated on the lines between the center of the field group and source group. The coupling effect of other directions can be ignored. Therefore, it is only necessary to calculate the coupling effect of the line between the center of the field group and the source group. Therefore, when the distance between the object and the environment meets the far-field approximate conditions, the use of FAFFA computation can greatly reduce the computation complexity, finally contributing to a higher computational efficiency.

4. Rough Sea Surface Model

4.1 PM Spectral Function

The PM spectral function under rectangular coordinates can be expressed as [29]

$$\begin{aligned} \mathrm{W}(K_{\mathrm{x}}, K_{\mathrm{y}}) = \frac{a}{2(K_x^2 + K_y^2)^2} \exp\left(-\frac{b g_0^2}{(K_x^2 + K_y^2) U_{19.5}^4} \right) \\ \cdot \frac{\cos^2\left[\tan^{-1}(K_{\mathrm{y}}/K_{\mathrm{x}}) - \phi_{\mathrm{m}} \right]}{\pi} \end{aligned} \tag{37}$$

where a and b are constants, and $a = 8.1 \times 10^{-3}$, $b = 0.74$, K_x and K_y represent the number of sea wave spaces, $U_{19.5}$ is the wind speed at a place 19.5 m from the sea surface and ϕ_m is the wind direction. When its value is zero, the wind direction is considered to be positive along the direction of x.

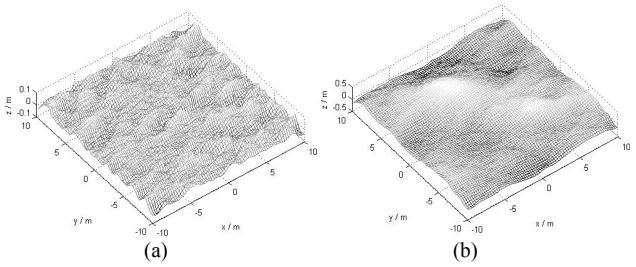

Fig. 2. The model of sea surface with different wind speed: (a) $U_{19.5} = 2$ m/s, (b) $U_{19.5} = 5$ m/s.

The root mean square (RMS) and correction length of the sea surface are

$$h_{\text{sea}} = \sqrt{\frac{a}{b}}\frac{U_{19.5}^2}{g_0} \approx 5.3325\times10^{-3}U_{19.5}^2, \tag{38}$$

$$l_{\text{sea}} = \frac{3\pi}{2}\sqrt{\frac{\pi}{2b}}\frac{U_{19.5}^2}{g_0} \approx 0.6999U_{19.5}^2. \tag{39}$$

As we see, the geometry of sea rough surface with different wind speed is shown in Fig. 2. Size of rough surface is $L_x \times L_y = 20$ m $\times$ 20 m; the wind speed of sea surface is $U_{19.5} = 2$ m/s and $U_{19.5} = 5$ m/s, respectively.

4.2 Seawater Permittivity Model

In order to truly reflect the permittivity of the actual sea surface, a double Debye seawater permittivity model [30] is used for simulation

$$\varepsilon = \frac{\varepsilon_S(T,S)-\varepsilon_1(T,S)}{1+\mathrm{j}f/f_1(T,S)} + \frac{\varepsilon_1(T,S)-\varepsilon_\infty}{1+\mathrm{j}f/f_2(T,S)} + \varepsilon_\infty - \mathrm{j}\frac{\sigma(T,S)}{(2\pi\varepsilon_0)f} \tag{40}$$

where T is seawater temperature, S is the salinity of seawater, f is the working frequency and σ is the ionic conductivity of seawater; ε, ε_S and ε_0 are the composite permittivity of seawater, static permittivity of seawater and permittivity in free space. ε_∞ is the seawater permittivity when the incident frequency tends to be infinite, which is taken as 4.9; $\varepsilon_1(T,S)$ is permittivity the of the mediate frequency; $f_1(T,S)$ and $f_2(T,S)$ are the first-order and second-order Debye relaxation frequencies, which can be expressed as

$$\begin{aligned} f_1(T,S) &= \frac{45+T}{a_1+a_2T+a_3T^2}\cdot\left[1+S\left(b_1+b_2T+b_3T^2\right)\right], \\ f_2(T,S) &= \frac{45+T}{a_4+a_5T+a_6T^2}\cdot\left[1+S\left(b_4+b_5T\right)\right] \end{aligned} \tag{41}$$

where a_i $(i = 1,\ldots,6)$ and b_k $(k = 1,\ldots,5)$ are the matching parameters of the tested value and the theoretically calculated value respectively.

Figure 3 shows the changes of the real part ε' and imaginary part ε'' of seawater permittivity along with the change of incident frequency, when the seawater temperature is 0°C, 10°C, 15°C and 20°C respectively. The salinity

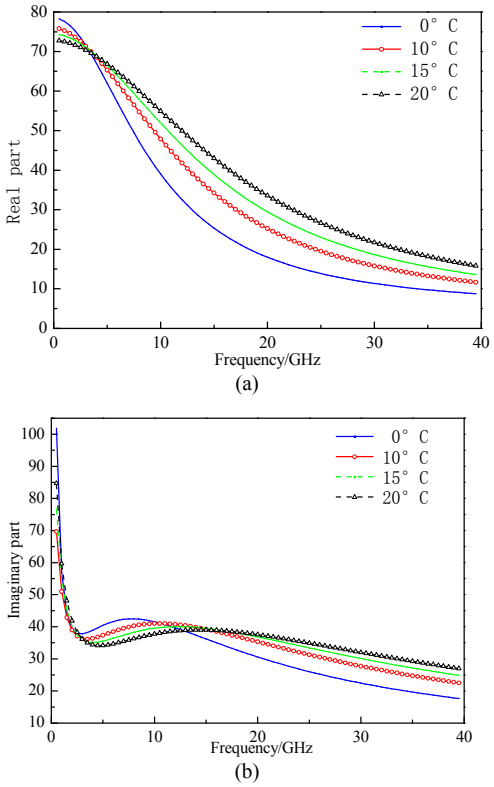

Fig. 3. Permittivity changes along with frequency at different temperatures: (a) real part changes with frequency, (b) imaginary part changes with frequency.

of seawater is 32.54‰. It can be seen from Fig. 3 that the real part of the permittivity gradually decreases along with the increase of frequency; the imaginary part decreases sharply in the low frequency band, and tends to stable in the high frequency band. The above means that the permittivity has a large loss in the low frequency band. When the irradiation frequency is below 3 GHz, the real part of the permittivity decreases along with the increase of temperature. When the irradiation frequency is above 3 GHz, it increases along with the increase of temperature. The imaginary part of the permittivity decreases along with the increase of temperature when the irradiation frequency is below 13 GHz but increases along with the increase of temperature when the irradiation frequency is above 13 GHz. Exact values under different parameters will be obtained in the following computations based on the permittivity model.

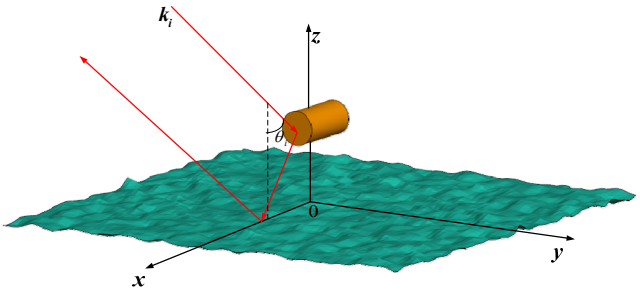

Fig. 4. A cylindrical object above the rough sea surface.

5. Results and Analysis of Numerical Computation

5.1 Algorithm Verification

In order to avoid the truncation error of the environment, the conical incident wave is used for irradiation. The expression of the conical incident wave is expressed as [31]

$$H^{\text{inc}}(x,y,z)=$$
$$-\frac{1}{\eta}\int_{-\infty}^{\infty}\mathrm{d}k_x\int_{-\infty}^{\infty}\mathrm{d}k_x\exp(\mathrm{i}k_x x+\mathrm{i}k_y y-\mathrm{i}k_z z)E_{\text{TE}}(k_x,k_y)\hat{h}(-k_z),$$
$$E^{\text{inc}}(x,y,z)=$$
$$\int_{-\infty}^{\infty}\mathrm{d}k_x\int_{-\infty}^{\infty}\mathrm{d}k_x\exp(\mathrm{i}k_x x+\mathrm{i}k_y y-\mathrm{i}k_z z)E_{\text{TE}}(k_x,k_y)\hat{e}(-k_z) \tag{42}$$

where

$$E_{\text{TE}}(k_x,k_y)=\frac{1}{4\pi^2}\int_{-\infty}^{\infty}\mathrm{d}x\int_{-\infty}^{\infty}\mathrm{d}y\Big[\exp(-\mathrm{i}k_x x-\mathrm{i}k_y y)\cdot\exp(\mathrm{i}(k_{ix}x+k_{iy}y)(1+w))\exp(-t)\Big], \tag{43}$$

$$t=t_x+t_y=(x^2+y^2)/g^2,$$
$$t_x=\frac{(\cos\theta_i\cos\varphi_i x+\cos\theta_i\sin\varphi_i y)^2}{g^2\cos^2\theta_i},$$
$$t_y=\frac{(-\sin\varphi_i x+\cos\varphi_i y)^2}{g^2}, \tag{44}$$
$$w=\frac{1}{k_0}\left[\frac{(2t_x-1)}{g^2\cos^2\theta_i}+\frac{(2t_y-1)}{g^2}\right]$$

where, g is the beam width, $g = L/4$

$$\hat{e}(-k_z)=\frac{1}{k_\rho}(\hat{x}k_y-\hat{y}k_x),$$
$$\hat{h}(-k_z)=\frac{k_z}{k_0k_\rho}(\hat{x}k_x-\hat{y}k_y)+\frac{k_\rho}{k_0}\hat{z}. \tag{45}$$

Figure 5 compares the improved hybrid algorithm with MoM, iterative MoM-PO and coupling MoM-PO algorithms by taking an example of a cylinder conductor above the rough sea surface. Table 1 further compares the computation time and memory consumption of different algorithms. The working frequency of radar is $f = 0.3$ GHz; five sampling points are taken for each wavelength; the incident angle is $\theta_i = 30°$, $\varphi_i = 0°$, the scattering angle is $\theta_s = -90° \sim 90°$, $\varphi_s = 0°$ and radius of a cylinder is $r = 1$ m and length of a cylinder is $l = 4$ m; the object height is $H = 5$ m, the temperature is 20° and the seawater permittivity is $\varepsilon = (72.49, 59.63)$; the size of rough sea surface is $L_x \times L_y$: 60×60 m^2; the sea surface wind speed is the first-level sea

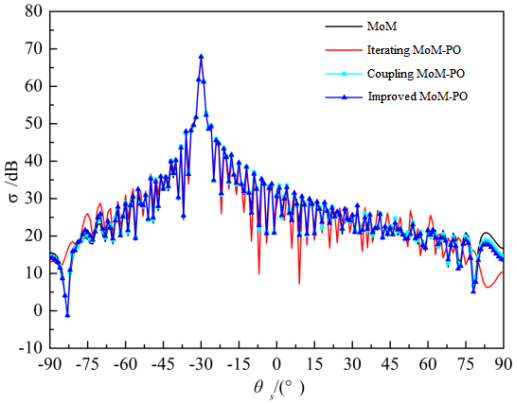

Fig. 5. Comparison of computation results by different algorithms (VV polarization).

Solver	MoM	Coupling MoM-PO	Improved MoM-PO
Memory consumption (MByte)	31270	1106	906
Computation time (s)	38033	17875	11082

Tab. 1. Comparison of computation time and memory consumption by different algorithms.

state. It can be found through comparison that the improved MoM-PO is basically consistent with the traditional coupling MoM-PO algorithm and MoM algorithm, which verifies the accuracy of the improved algorithm. By comparing the computation time and memory occupied by different algorithms, the improved hybrid algorithm can significantly improve the computation rate compared with the traditional coupling MoM-PO algorithm.

5.2 Change of Composite Scattering Characteristics with Object Spacing

The change of composite scattering characteristics along with object spacing is shown in Fig. 6, where the object spacing is $d = 1$ m, $d = 3$ m, $d = 5$ m, the size of cylinder is $\pi\lambda^2 \cdot l : 1.0^2 \times 4\pi$ m^3 and the number of objects is 3; the incident angle is $\theta_i = 30°$, $\varphi_i = 0°$ and the scattering angle is $\theta_s = -90° \sim 90°$, $\varphi_s = 0°$; the sea surface wind

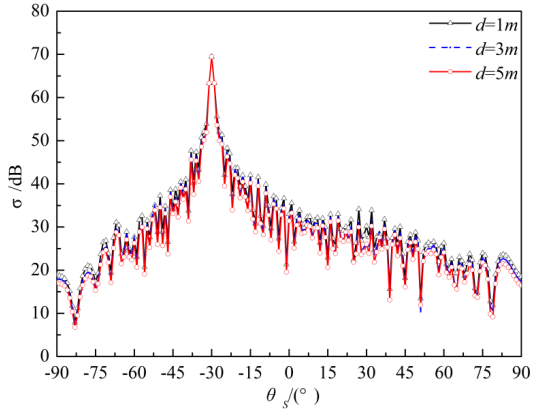

Fig. 6. Change of composite scattering coefficient with the object spacing.

speed is the first-level sea state, the temperature is 20° and the seawater permittivity is $\varepsilon = (72.49, 59.63)$. As shown in the figure, the peak value of composite scattering coefficient appears in the –30° direction, and the peaks corresponding to different object spacing are exactly the same, which implies that the object spacing exerts little influence on the radial direction object and environment coupling effect. In most scattering directions except the radial direction, the larger the object spacing is, the smaller the composite scattering coefficient will be, because the coupling effect between the objects decreases along with the increase of object spacing, which leads to the decrease of the composite scattering coefficient.

5.3 Change of Composite Scattering Characteristics with Object Size

The change of the composite scattering coefficient with object size is shown in Fig. 7, where the size of cylinder object is $\pi\lambda^2 \cdot l$: $0.5^2 \times 2\pi$ m^3, $\pi\lambda^2 \cdot l$: $1.0^2 \times 4\pi$ m^3 and $\pi\lambda^2 \cdot l$: $1.5^2 \times 6\pi$ m^3, the object spacing is $d = 3$ m and the number of objects is 3; the incident angle is $\theta_i = 30°$, $\varphi_i = 0°$ and the scattering angle is $\theta_s = -90° \sim 90°$, $\varphi_s = 0°$; the sea surface wind speed is the first-level sea state, the temperature is 20° and the seawater permittivity is $\varepsilon = (72.49, 59.63)$. As shown in the figure, the peak of composite electromagnetic scattering coefficient appears at –30°, and the peaks corresponding to different composite scattering coefficients are exactly the same; in most scattering directions except the radial direction, the larger the object size is, the more larger the overall composite scattering coefficient and the more obvious the backscattering will be, because the coupling between the object and the environment exerts little influence on the composite scattering in the radial direction. The larger the object size is, the stronger the electromagnetic coupling between the object and the environment will be. The above contributes to a higher overall composite scattering coefficient. The more obvious backscattering reflects the strength of the coupling between the object and the environment. The greater the backscattering is, the stronger the coupling effect will be.

5.4 Changes of Composite Scattering Characteristics with the Tilt Angle of the Object

The change of composite scattering coefficient with the tilt angle of the object is shown in Fig. 8, where the downward tilt angle of the cylinder around the particle is 30°, 60° and 90°. The incident angle is $\theta_i = 30°$, $\varphi_i = 0°$ and the scattering angle is $\theta_s = -90° \sim 90°$, $\varphi_s = 0°$; the size of cylinder is $\pi\lambda^2 \cdot l$: $1.0^2 \times 4\pi$ m^3, the object spacing is $d = 3$ m and the number of objects is 3; the sea surface wind speed is the first-level sea state, the temperature is 20° and the seawater permittivity is $\varepsilon = (72.49, 59.63)$. As shown in the figure, the peak appears in the –30° direction and the peak value is basically the same under different rotation angles of the object; in the backscattering direction, the scattering coefficient is the strongest and the weakest respectively when the tilt angle of cylinder is 60° and 30°; in the direction of large scattering angle, the coefficient is the strongest when the tilt angle is 30° because when the tilt angle of object is 60°, the incident wave irradiates the object vertically, and the object is irradiated by the incident wave with the greatest intensity. As a result, the coupling effect with the environment is the strongest, causing the largest backscattering coefficient. At the same time, when the tilt angle of object is 30°, the amplitude of composite scattering coefficient is strong along the large scattering angle due to the reflection of object surface and edge diffraction.

5.5 Change of Composite Scattering Characteristics with Object Type

The change of composite scattering coefficient with the object type is shown in Fig. 9, where the object types are cuboid, cylinder and circular cone, the size of which is $l \times l \times l$: $2 \times 2 \times 4$ m^3, $\pi r^2 \times l$: $\pi \times 1^2 \times 4\pi$ m^3 and $1/3\pi r^2 \cdot l$: $1/3\pi \times 1^2 \times 4$ m^3 respectively; the incident angle is $\theta_i = 30°$, $\varphi_i = 0°$, the scattering angle is $\theta_s = -90° \sim 90°$, $\varphi_s = 0°$; the sea

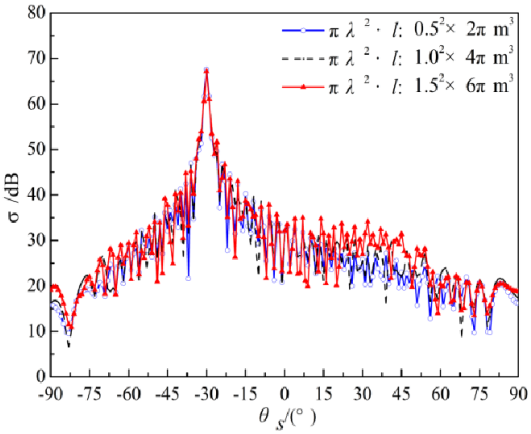

Fig. 7. Changes of composite scattering coefficient with object size.

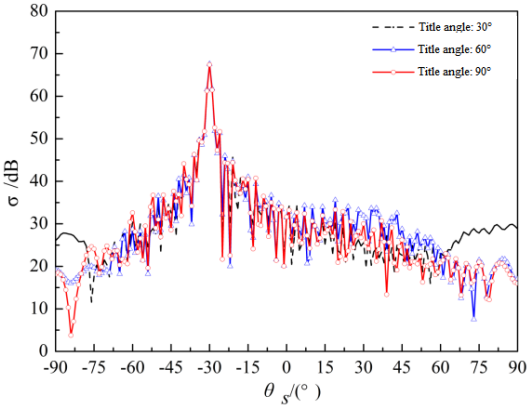

Fig. 8. Change of composite scattering coefficient with the tilt angle of the object.

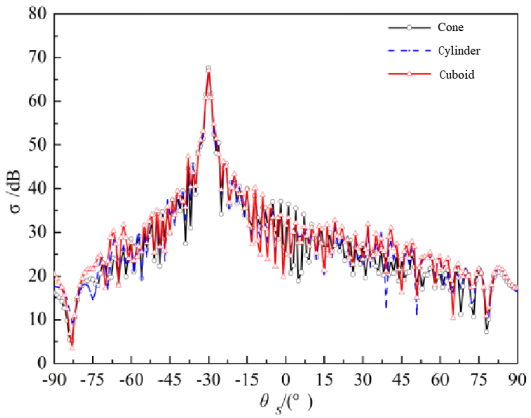

Fig. 9. Change of composite scattering coefficient with the object type.

surface wind speed is the first-level sea state, the temperature is 20° and the seawater permittivity is $\varepsilon = (72.49, 59.63)$. As shown in the figure, when the object type is a cuboid, the scattering coefficient is the largest and the backscattering is the strongest, followed by the object of cylinder type. When the object is a circular cone, the scattering coefficient is the smallest and the backscattering is the weakest. When the object is a cuboid, the size is larger, bringing stronger coupling effect and larger backscattering coefficient. When the object is a cone, the composite scattering coefficient in the direction of –7.5° ~ 7.5° is stronger than that when the object is a cuboid and a cylinder. The above is mainly ascribed to the diffraction of the circular cone point.

5.6 Change of Composite Scattering Characteristics with Different Incident Angles

The change of composite scattering coefficient with different incident angles is shown in Fig. 10, where the incident angles are $\theta_i = 30°$, $\varphi_i = 0°$, $\theta_i = 30°$, $\varphi_i = 45°$ and $\theta_i = 30°$, $\varphi_i = 90°$. The size of cylinder is $\pi\lambda^2 \cdot l$: $1.0^2 \times 4\pi$ m^3; the sea surface wind speed is the first-level sea state, the

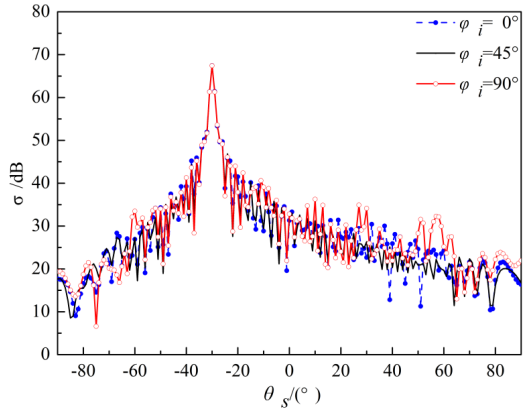

Fig. 10. Change of composite scattering coefficient with different incident angles.

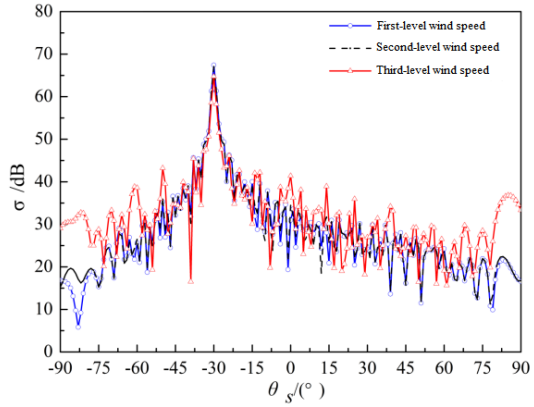

Fig. 11. Change of composite scattering coefficient with sea surface wind speed.

temperature is 20° and the seawater permittivity is $\varepsilon = (72.49, 59.63)$. As shown in the figure, when the incident angle is $\theta_i = 30°$, $\varphi_i = 90°$ and the overall composite electromagnetic scattering coefficient is the largest. In the backscattering direction, when the incident azimuth is $\varphi_i = 90°$, the scattering is the strongest, and has multiple peaks; when the incident azimuth is $\varphi_i = 45°$, the backscattering coefficient is the weakest. This is mainly because when the incident azimuth is $\varphi_i = 90°$, the object has the largest irradiated area, bringing the largest scattering coefficient; because of multiple objects, there are multiple different peaks at different angles in the backscattering direction. When the incident azimuth is $\varphi_i = 45°$, its relative scattering cross section is the smallest.

5.7 Change of Composite Scattering Characteristics with Sea Surface Wind Speed

The change of composite scattering coefficient with sea surface wind speed is shown in Fig. 11. The sea surface wind speeds are first-level, second-level and third-level state respectively. The object type is cylinder, the size of which is $\pi r^2 \times l$: $\pi \times 1^2 \times 4$ m^3. The incident angle is $\theta_i = 30°$, $\varphi_i = 0°$, the scattering angle is $\theta_s = –90° \sim 90°$ and the ambient temperature is 20°; the seawater permittivity is $\varepsilon = (72.49, 59.63)$. As shown in the figure, the peak appears in the –30° direction; the greater the sea surface wind speed, the smaller the peak. In most scattering directions except the radial direction, the greater the sea surface wind speed, the greater the composite electromagnetic scattering coefficient, because the peak of the radial scattering direction is mainly caused by coherent scattering. The greater the sea surface wind speed, the weaker the coherent scattering, leading to a weaker coupling effect in the radial direction and reduction of the composite scattering coefficient. The increase of sea surface wind speed also increases the diffuse reflection of the environment and the coupling between the object and the rough sea surface, leading to the increase of the overall composite scattering coefficient.

6. Conclusion

Oriented to the composite scattering from 3D conductor multi-objects above environment, this paper makes computation based on the hybrid algorithm integrated with method of moment and physical optic method and obtains the composite electromagnetic scattering coefficient by accelerating the coupling effect between object area and rough surface area in virtue of the MLFMA-FAFFA. This paper establishes a composite scattering model of coupling MoM-PO and deduces the formula of MLFMA-FAFFA in detail. In addition, the changes of composite scattering characteristics from the 2D sea surface and the 3D multi-objects with the object spacing, size, type, tilt angle, incident angle of the irradiated wave and sea surface wind speed are also analyzed in detail. The results show that the object spacing, type, tilt angle, etc. exert significant influence on the composite electromagnetic scattering characteristics from object above the rough surface. The simulation results serve as important basis for identifying and judging object parameters and characteristics. The higher accuracy and computation efficiency of the improved hybrid algorithm are also verified by comparing with the MoM algorithm and the traditional MoM-PO hybrid algorithm.

References

[1] ZAMANI, H., TAVAKOLI, A., DEHMOLLAIAN, M. Scattering from layered rough surfaces: Analytical and numerical investigations. *IEEE Transactions on Geoscience and Remote Sensing*, 2016, vol. 54, no. 6, p. 3685–3696. DOI: 10.1109/TGRS.2016.2524639

[2] WEI, P., TEKIC, J., YANG, Y., et al. The friction phenomena in underdamped three layers Frenkel–Kontorova model. *Waves in Random and Complex Media,* 2016. vol. 26, no 4, p. 592–598. DOI: 10.1080/17455030.2016.1179354

[3] XU, R. W., GUO, L. X., HE, H. J., et al. A hybrid FEM/MoM technique for 3-D electromagnetic scattering from a dielectric object above a conductive rough surface. *IEEE Geoscience and Remote Sensing Letters*, 2016, vol. 13, no. 3, p. 314–318. DOI: 10.1109/LGRS.2015.2508500

[4] MARTINO, G. D., IODICE, A., RICCIO, D., et al. Ocean monitoring with SAR: An overview. In *IEEE OCEANS 2015*. Genova (Italy), 2015, p. 1–5. DOI: 10.1109/OCEANS-Genova.2015.7271622

[5] XIE, T., PERRIE, W., ZHAO, S. Z., et al. Electromagnetic backscattering from one-dimensional drifting fractal sea surface II: Electromagnetic backscattering model. *Chinese Physics B,* 2016, vol. 25, no. 7, p. 1–6.

[6] KIM, K., KIM, J. H., CHO, D. S. Radar cross section analysis of marine targets using a combining method of physical optics/geometric optics and a Monte-Carlo simulation. *Ocean Engineering*, 2009, vol. 36, no. 11, p. 821–830. DOI: 10.1016/j.oceaneng.2009.05.005

[7] BAKR, S. A., MANNSETH, T. An approximate hybrid method for electromagnetic scattering from an underground target. *IEEE Transactions on Geoscience & Remote Sensing*, 2013, vol. 51, no. 1, p. 99–107. DOI: 10.1109/TGRS.2012.2198068

[8] REN, X. C., ZHU, X. M., LIU, P., et al. Wide-band composite electromagnetic scattering from the earth soil surface and multiple targets shallowly buried. *Acta Physica Sinica,* 2016. vol. 65, p. 1–9. (In Chinese) DOI: 10.7498/aps.65.204101

[9] WANG, X., GAN, Y. B., LI, L. W. Electromagnetic scattering by partially buried PEC cylinder at the dielectric rough surface interface: TM case. *IEEE Antennas & Wireless Propagation Letters*, 2003, vol. 2, p. 319–322. DOI: 10.1109/LAWP.2003.822200

[10] HESTENES, M. R., STIEFEL, E. L. Methods of conjugate gradients for solving linear systems. *Journal of Research of the National Bureau of Standards (United States*), 1952, vol. 49, no. 6, p. 409–436. DOI: 10.6028/jres.049.044

[11] JIN, Y. Q., LI, Z. Numerical simulation of radar surveillance for the ship target and oceanic clutters in two-dimensional model. *Radio Science,* 2003, vol. 38, no. 3, p. 1–6. DOI: 10.1029/2002RS002692

[12] EL-SHENAWEE, M., RAPPAPORT, C. M. Monte Carlo simulations for clutter statistics in minefields: AP-Mine-Like-Target buried near a dielectric object beneath 2-D random rough ground surfaces. *IEEE Transactions on Geoscience & Remote Sensing*, 2002. vol. 40, no. 6, p. 1416–1426. DOI: 10.1109/TGRS.2002.800275

[13] STUTZMAN, W. L., THIELE, G. A. *Antenna Theory and Design,* New York: John Wiley and Son*,* 1998. ISBN: 0471025909

[14] KOUYOUMJIAN, R. G., PATHAK, P. H. A uniform geometrical theory of diffraction for an edge in a perfectly conducting surface. *Proceedings of the IEEE*, 1974, vol. 62, no. 11, p. 1448–1461. DOI: 10.1109/PROC.1974.9651

[15] LING, H., CHOU, R. C., LEE, S. W. High frequency RCS of open cavities with rectangular and circular cross sections. *IEEE Transaction and Antennas Propagations*, 1989, vol. 37, no. 5, p. 648–654. DOI: 10.1109/8.24193

[16] BURKHOLDER, R. J., TOKGOZ, C., REDDY, C. J., et al. Iterative physical optics for radar scattering predictions. *Application Computation Electromagnetic Society Journal,* 2009, vol. 24, no. 2, p. 241–258. ISSN: 10544887

[17] RASHIDI-RANJBAR, E., DEHMOLLAIAN, M. Target above random rough surface scattering using a parallelized IPO accelerated by MLFMM. *IEEE Geoscience & Remote Sensing Letters,* 2015, vol. 12, no. 7, p. 1481–1485. DOI: 10.1109/LGRS.2015.2409555

[18] XIANG, D. P., BOTHA, M. M. MLFMM-based, fast multiple-reflection physical optics for large-scale electromagnetic scattering analysis. *Journal of Computational Physics*, 2018, vol. 368, p. 69 to 91. DOI: 10.1016/j.jcp.2018.04.054

[19] RUI, W., GUO, L., QIN, S., et al. Hybrid method for investigation of electromagnetic scattering interaction between the conducting target and rough sea surface. *Acta Physica Sinica*, 2008, vol. 57, no. 6, p. 3473–3480. (In Chinese) DOI: 10.7498/aps.57.3473

[20] ZHANG, Y., YANG, Y. E., BRAUNISCH, H., et al. Electromagnetic wave interaction of conducting object with rough surface by hybrid SPM/MOM technique. *Journal of Electromagnetic Waves and Applications*, 1999, vol. 13, no. 7, p. 983–984. DOI: 10.1163/156939399X00457

[21] LI, J., GUO, L. X., HE, Q. Hybrid FE-BI-KA method in analysing scattering from dielectric object above sea surface. *Electronics Letters*, 2011, vol. 47, no. 20, p. 1147–1148. DOI: 10.1049/el.2011.1444

[22] LI, J., LI, K., GUO, L. X., et al. A hybrid IEM–PO method for composite scattering from a PEC object above a dielectric sea surface with large wind speed: HH polarization. *Waves in Random & Complex Media*, 2017, vol. 28, no. 4, p. 630–642. DOI: 10.1080/17455030.2017.1380333

[23] YE, H., JIN, Y. Q. A hybrid KA-MoM algorithm for computation of scattering from a 3-D PEC target above a dielectric rough surface. *Radio Science,* 2008, vol. 43, no. 3, p. 1–15. DOI: 10.1029/2007RS003702

[24] WEI, T., REN, X. C., GUO, L. X. Study on composite electromagnetic scattering from the double rectangular cross-section columns above rough sea surface using hybrid method. *Acta Physica Sinica,* 2015, vol. 64, no. 17, p. 1–6. (In Chinese) DOI: 10.7498/aps.64.174101

[25] TIAN, G. L., TONG, M. C., LIU, H., et al. An improved MoM-PO hybrid method for scattering from multiple 3D targets above the 2D random conducting rough surface. *Electromagnetics,* 2019, vol. 39, no. 5, p. 375–392. DOI: 10.1080/02726343.2019.1619231

[26] CHEW, W. C., CUI, T. J., SONG, J. M. A FAFFA-MLFMA algorithm for electromagnetic scattering. *IEEE Transactions on Antennas and Propagation*, 2002, vol. 50, no. 11, p. 1641–1649. DOI: 10.1109/TAP.2002.802162

[27] LIU, Z. L., WANG, C. F. Efficient iterative Method of Moments—Physical Optics hybrid technique for electrically large objects. *IEEE Transactions on Antennas & Propagation*, 2012, vol. 60, no. 7, p. 3520–3525. DOI: 10.1109/TAP.2012.2196963

[28] SONG, J. M., LU, C. C., CHEW, W. C. et al. Multilevel fast multipole algorithm for electromagnetic. *IEEE Transactions on Antennas & Propagation*, 1997, vol. 45, no. 10, p. 1488–1493. DOI: 10.1109/8.633855

[29] FRANCESCHETTI, G., IODICE, A., MIGLIACCIO, M., et al. Scattering from natural rough surfaces modeled by fractional Brownian motion two-dimensional processes. *IEEE Transactions on Antennas & Propagation*, 1999, vol. 47, no. 9, p. 1405–1415. DOI: 10.1109/8.793320

[30] MEISSNER, T., WENTZ, J. The complex dielectric constant of pure and sea water from microwave satellite observations. *IEEE Transactions on Geoscience & Remote Sensing*, 2004, vol. 42, p. 1836–1849. DOI: 10.1109/TGRS.2004.831888

[31] TSANG, L., KONG, J. A., DING, K. H., et al. *Scattering of Electromagnetic Waves: Numerical Simulations*. New York: John Wiley & Sons, 2001, p. 278. DOI: 10.1002/0471224308

About the Authors ...

Ting LIU was born in Hunan Province, People's Republic of China in 1981. She received the B.S degree in Management from the Hunan Agricultural University in 2003, and the M.S. degree from Xiangtan University in 2010. She is presently working towards her Ph.D. degree at the Air Force Engineering University, Xi'an, ShanXi. Her main research interest is the theory and technology of radar anti-jamming. Her email is: gltian163@163.com

Lin ZHANG graduated from the School of Air Defense and Missile Defense of China Air Force Engineering University with a Master of Science degree and a doctor's degree. He has published more than 60 scientific papers in his field. His interests include fault diagnosis, systems engineering, and fault diagnosis and health management.

Zhiguo ZENG was born in Hunan Province, People's Republic of China in 1977. He received the B.S degree in Computer Science and Technology from the Hunan Normal University in 2000, and the M.S. degree from the Central South University in 2011. He is presently working towards his Ph.D. degree at the Air Force Engineering University, Xi'an, ShanXi. His main research interests are deep learning in convolutional neural network and computer vision. His email is: 9203646@qq.com

Shengjun WEI was born in Shandong Province in 1983. In 2008, he received a bachelor's degree in early warning detection from the Air Force Early Warning Academy, and a master's degree in equipment science from the Air Force Engineering University in 2020. His research interests include the contribution rate of equipment system. His email address is: 324180447@qq.com